Check for updates

Wiley
Structural Control and Health Monitoring
Volume 2025, Article ID 9780866, 20 pages
https://doi.org/10.1155/stc/9780866

WILEY

Research Article

Automatic Identification of Diverse Tunnel Threats With Machine Learning–Based Distributed Acoustic Sensing

Taiyin Zhang,[1,2] Cheng-Cheng Zhang,[1] Tao Xie,[1] Xiaomin Xu,[2,3] and Bin Shi[1]

[1]*School of Earth Sciences and Engineering, Nanjing University, Nanjing 210023, China*
[2]*Department of Engineering, University of Cambridge, Cambridge CB3 0FA, UK*
[3]*School of Engineering, The University of Manchester, Manchester M13 9PL, UK*

Correspondence should be addressed to Cheng-Cheng Zhang; zhang@nju.edu.cn and Bin Shi; shibin@nju.edu.cn

Received 14 July 2024; Accepted 4 April 2025

Academic Editor: Sara Casciati

Copyright © 2025 Taiyin Zhang et al. Structural Control and Health Monitoring published by John Wiley & Sons Ltd. This is an open access article under the terms of the Creative Commons Attribution License, which permits use, distribution and reproduction in any medium, provided the original work is properly cited.

As the backbone of modern urban underground traffic space, tunnels are increasingly threatened by natural disasters and anthropogenic activities. Current tunnel surveillance systems often rely on labor-intensive surveys or techniques that only target specific tunnel events. Here, we present an automated tunnel monitoring system that integrates distributed acoustic sensing (DAS) technology with ensemble learning. We develop a fiber-optic vibroacoustic dataset of tunnel disturbance events and embed vibroscape data into a common feature space capable of describing diverse tunnel threats. On the scale of seconds, our anomaly detection pipeline and data-driven stacking ensemble learning model enable automatically identifying nine types of anomalous events with high accuracy. The efficacy of this intelligent monitoring system is demonstrated through its application in a real-world tunnel, where it successfully detected a low-energy but dangerous water leakage event. The highly generalizable machine learning model, combined with a universal feature set and advanced sensing technology, offers a promising solution for the autonomous monitoring of tunnels and other underground spaces.

1. Introduction

Underground infrastructure constitutes the backbone of the economic life of modern cities [1]. Tunnels are important underground transportation spaces [2]. With the development of ultra-deep and ultra-long tunnels, and due to the complexity of geologic conditions and various anthropogenic activities, tunnels are increasingly threatened by a range of disasters such as groundwater inflows, rock bursts, rockfalls, and tunnel breakdown [3, 4], during both construction and operation. Therefore, ensuring the secure construction and operation of tunnels, as well as the timely anticipation of impending risks, requires diligent monitoring and assessment of the safety and stability status of the tunnels.

On-site monitoring for tunnel safety is broadly divided into contact and noncontact techniques [5]. Contact methods utilize physical point sensors attached to the tunnel structure to evaluate stability and safety [6]. For example, microseismic monitoring employs seismic sensors to detect microseismic activities in the surrounding rock mass, providing early warnings of tunnel rockburst disasters [7]. Strain gauges measure strain changes within tunnel structures, highlighting potential issues such as stress concentrations or cracks [8]. Temperature sensors identify leakage events by monitoring temperature variations of tunnel lining segments [9]. However, these point-based methods can fail to detect localized issues that develop between sensor placements, potentially leading to unnoticed structural weaknesses [10]. Furthermore, once installed, contact sensors are stationary and cannot be easily relocated, limiting their adaptability to evolving tunnel conditions. Contactless methods include vision-based methods (e.g., digital photogrammetry [11], robot inspections [12]), acoustic techniques [13], three-dimensional laser scanning [14], and infrared thermographic monitoring [15]. Despite providing

high-precision data, noncontact methods face challenges such as high equipment costs, complex data processing requirements, and susceptibility to rapidly changing environmental conditions within tunnels. For example, vision-based and laser-based techniques can be compromised by dust, water vapor, or other particulate matter, which scatter or absorb signals, thereby degrading data quality and complicating the differentiation of true structural changes from noise [12]. While traditional tunnel monitoring methods, including threshold-based detection, frequency-domain analysis, and statistical models, have been widely used, they often require manual tuning and rely on predefined parameters, making them sensitive to noise and environmental variability. These methods typically extract single features, which may not fully capture the complexity of distributed acoustic sensing (DAS) signals. Despite significant advancements, no current method achieves the desired level of real-time monitoring and spatial resolution necessary for comprehensive and diverse threat identification in tunnel environments.

Recently, DAS—a fiber-optic sensing technology that allows for dense large-aperture vibroacoustic measurements [16, 17]—has emerged rapidly as a powerful tool for perimeter security surveillance, oil and gas well diagnosis, and seismic observation and imaging [18–21]. Based on the principle of phase-sensitive optical time-domain reflectometry (ϕ-OTDR), DAS can perform array measurements of vibrations over tens of kilometers of common fiber-optic cable with high sensitivity and reliability, potentially enabling time-lapse monitoring of tunnel safety by characterizing its "vibroscape"—a term used to describe the overall characteristics of environmental vibration signals [22]. This approach integrates various disturbance events into a unified feature space, allowing for comprehensive threat analysis. DAS has excellent reliability and anti-interference performance. By incorporating specially designed sheaths, the optical fibers can operate in diverse environmental conditions, including high temperatures, high humidity, and high pressure, making DAS well suited for complex tunnel environments.

A striking feature of DAS-based vibroacoustic monitoring is that the sensing fiber array is interrogated at a channel spacing of the order of decimeters, leading to data volumes that are tens to hundreds of times larger than the traditional point-wise microseismic monitoring. For example, a field experiment on a 20-km dark fiber cable (sampled at 500 Hz) has collected about 12 terabytes of data over a period of 40 days [23]. Such acquisition fashions and datasets challenge current models of data storage, transmission, and analysis, thus hindering real-time monitoring and immediate decision-making. Therefore, it is an urgent task to develop a common framework that can efficiently handle huge volumes of DAS data, especially to automatically detect and rapidly identify anomalies in noisy environments.

An appealing strategy for DAS data processing and event recognition is to use machine learning [24]. Yet to date, most machine learning–based DAS studies reported have used only one algorithm (e.g., support vector machine [SVM], eXtreme gradient boosting [XGBoost], and random forest [RF]) for classification [25–27], and comparative studies have mostly employed a reduced set of fiber-optic vibrational events (mostly three-class classification problems) that cover limited ground and geographical conditions [28, 29]. There is no conclusive answer as to which machine learning algorithm has the best predictive performance for DAS-recorded engineering vibroacoustic signals. Importantly, so far, there are a very few reported research efforts [30] that are dedicated to tunnel condition monitoring. Models built for other scenarios may not be directly applicable to tunnel environments, as there can be significant differences in the best machine learning strategy and the most predictive feature set.

This study includes the following three contributions: (1) we proposed a novel integrated framework for automated tunnel threat monitoring using machine learning and DAS-recorded vibroscapes. Our approach also includes an effective anomaly detection pipeline including signal picking, separation, and filtering to extract vibration signals from random background noise. (2) We developed a publicly available DAS dataset of tunnel vibrational events. We selected highly predictive features of vibration signals to describe diverse tunnel threats, focusing on time- and frequency-domain properties. (3) We performed DAS measurements of vibrational events in the Beijing–Xiong'an (Jing–Xiong) intercity railway tunnel (Hebei, China) to validate the proposed approach. Our system successfully identified events such as leakage, excavation activities, and vehicle passage with high accuracy.

The remainder of this paper is organized as follows. Section 2 details the architecture of the proposed ML-based DAS monitoring system. Section 3 describes the methods used for dataset acquisition from real tunnels. Section 4 presents the outcomes of training and evaluation, including the impact of key factors. Section 5 showcases the application of our system in the Jing–Xiong intercity railway tunnel. Section 6 provides a summary of this paper and discusses future directions for using DAS in tunnel safety monitoring.

2. Methodology

2.1. Overview. As illustrated in Figure 1, we present a novel framework for the automated monitoring of tunnel disturbance events using machine learning and DAS-recorded vibroscapes. The framework consists of three subsystems: anomaly detection, feature selection, and multiclass recognition. In the anomaly detection subsystem, we utilize the improved STA/LTA method along with the normalized cumulative energy curve to swiftly and accurately identify tunnel vibration events from extensive real-time DAS background noise. Subsequently, the signal denoising algorithm is employed to denoise the vibration signals, enhancing the signal-to-noise ratio (SNR). Regarding feature selection, the elastic net algorithm is employed to circumvent collinearity and reduce the dimensionality of the feature space, thereby selecting high-quality features for subsequent classification. The third subsystem is a machine

schm, 2025, 1, Downloaded from https://onlinelibrary.wiley.com/doi/10.1155/stc/9780866 by Cochrane Czech Republic, Wiley Online Library on [21/03/2026]. See the Terms and Conditions (https://onlinelibrary.wiley.com/terms-and-conditions) on Wiley Online Library for rules of use; OA articles are governed by the applicable Creative Commons License

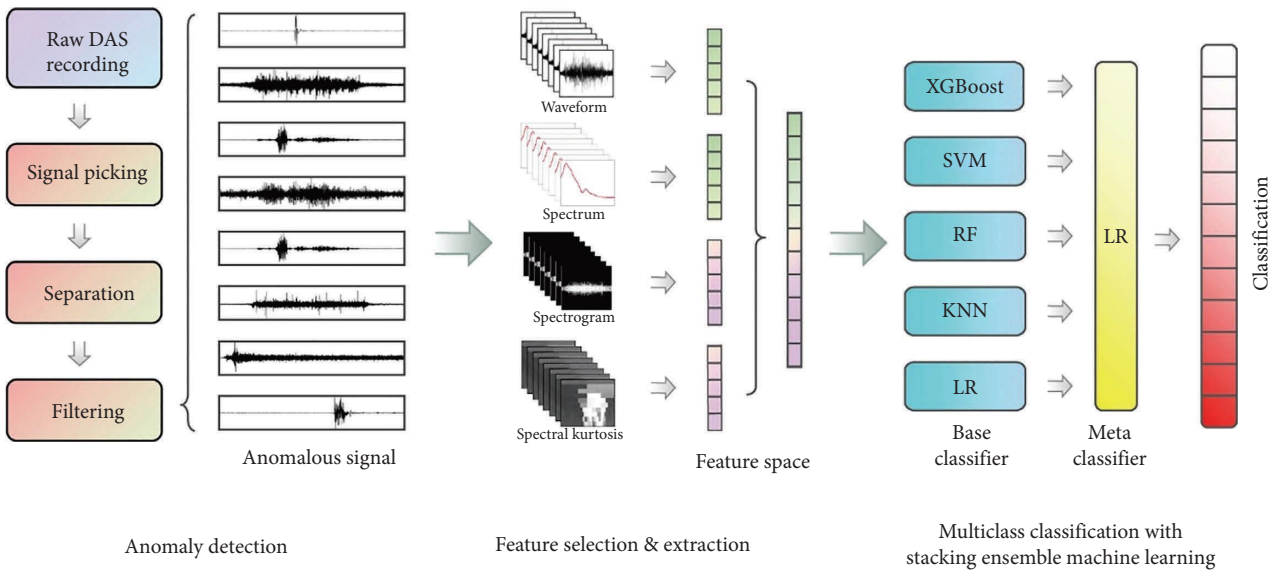

FIGURE 1: The framework of the DAS monitoring system for automatic tunnel threat identification.

learning–based automatic classification module. We employ a stacking ensemble learning strategy to train and optimize a combination of well-performing classification algorithms with our feature set through cross-validation [31].

2.2. Automated Anomaly Detection

2.2.1. Self-Adjusted Signal Picking and Separation Procedures. The first part of our intelligent DAS monitoring system is an anomaly detection subsystem that automatically detects and separates tunnel irregular events. To pick abnormal vibration signals from ambient DAS recordings, we used an improved short-term average over long-term average (STA/LTA) algorithm with dynamic thresholds that differentiate signals from background noise based on their energy level. This tool works by comparing the average energy of the STA leading window and the LTA trailing window, which can be expressed by

$$R(i) = \frac{\mathrm{STA}(i)}{\mathrm{LTA}(i)} = \frac{\sum_{j=i-s}^{i} CF(i)/s}{\sum_{j=1}^{i+1} CF(i)/l} - 1, \quad (1)$$

$$\mathrm{CF}(i) = |Y(i+1) - Y(i)|, \quad (2)$$

where R is the average energy ratio of the STA window to the LTA window; i is the time index; s and l are the lengths of the STA and LTA windows, respectively; CF is the characteristic function; and Y is the signal amplitude. In the absence of an event, both STA and LTA are influenced by the background noise level, producing an STA/LTA ratio close to 0 [32]. When an abnormal event occurs, the STA value changes dramatically, while the LTA value remains stable, resulting in an STA/LTA ratio greater than 0. When the ratio between these two averages is found to be higher than a predefined limit, an event is detected.

The duration of the detected signal can be measured by dual-thresholding in the STA/LTA algorithm. The low threshold sensitively captures the energy change of the time series and preliminarily obtains the initiation point of the signal. However, there are two cases that can trigger a low threshold including the onset of the signal and accidental high-energy noise, making further classification via high thresholding necessary. The signal is considered to trigger on only when the STA/LTA ratio reaches the high threshold and lasts for at least 0.01 s. And if the STA/LTA ratio of this moment and the following five sliding windows are simultaneously less than the low threshold, the signal can be triggered off. Finally, we add 1 second of data before and after the duration to ensure the completeness of the signal. In addition, weather affects transportation [33] and topsoil conditions, which in turn biases the SNR of the same event. Therefore, the low threshold is dynamically adjusted to suppress the impact of environmental noise. Every hour, the system calculates a logarithmic root-mean-square (RMS) ratio of a 5-second background noise to the standard noise and integrates that ratio to the low threshold. A noisier environment produces a positive ratio, while a quieter environment produces a negative ratio; this enables dynamic fine-tuning of the base threshold. In this manner, false triggering on noisy signals can be minimized.

To extract the detected signals from the ambient vibration recordings while discarding unwanted data, we used the normalized cumulative energy curve [34], which allowed us to separate the signals of interest from the background noise in real time. Based on the interval extracted by STA/LTA, the trigger on/off of an event can be accurately computed by setting any two fractions of the normalized cumulative integral curve of the squared signal amplitude. In this work, we use 0.5% and 99.5% of the maximum to determine the start–stop points.

By combining these two algorithms, we can separate the detected signal from the background noise in real time. In this way, only signals of tunnel-disturbing events are left, while large, redundant DAS data are discarded.

schm, 2025, 1, Downloaded from https://onlinelibrary.wiley.com/doi/10.1155/stc/9780866 by Cochrane Czech Republic, Wiley Online Library on [21/03/2026]. See the Terms and Conditions (https://onlinelibrary.wiley.com/terms-and-conditions) on Wiley Online Library for rules of use; OA articles are governed by the applicable Creative Commons License

2.2.2. Signal Denoising Methods. Our system next eliminates potential noise in the extracted signals, as their quantitative parameters can be biased by low SNRs. To achieve the best denoising performance, we evaluated four frequency-domain filters, namely, empirical mode decomposition (EMD), complementary ensemble empirical mode decomposition (CEEMD), variational mode decomposition (VMD), and wavelet threshold denoising (WTD). Among them, VMD and WTD are known as powerful denoisers with rich sets of adjustable parameters [35, 36], while EMD and CEEMD have relatively fewer parameters [37, 38] Time-domain filters that act essentially as data smoothers were not included in this comparison because they are very time-consuming and may ignore subtle variations in signal details. In addition, we did not consider band-pass filtering because it requires an a priori knowledge of the frequency attributes of signals and ignores time effects. Three metrics—SNR, root-mean-square error (RMSE), and smoothness—were used to quantitatively assess these methods. The parameter settings of the denoising algorithms are given in Table 1.

2.3. Elastic-Net Regression for Feature Selection. After signal denoising, the multithreat monitoring system automatically extracts signal features and then passes them to the machine learning–based pattern recognition subsystem. To construct a common, highly descriptive feature set for diverse tunnel vibration events, we examined a wide range of signal features [39]. We initially screened 11 waveform features, 4 spectral features, 5 spectrogram features, and 4 spectral kurtosis features, totaling 24 features (Table 2).

To avoid collinearity and reduce dimensionality of our feature space, we combined heatmap correlation analysis with elastic-net regression to perform a feature selection for the 24 signal features. Elastic-net [40] is a regularized regression method that linearly combines both penalties (i.e., L1 and L2) of the Lasso and Ridge regression methods: the L1 penalty ensures the sparsity of the estimator, while the L2 penalty improves the stability of the model. The objective function of elastic-net takes the following form of "loss + penalty":

$$\min_{\beta_0,\beta} \frac{1}{n}\sum_{i=1}^{n} w_i l\left(y_i, \beta_0 + \beta^T x_i\right) + \lambda\left(\frac{(1-\alpha)\|\beta\|_2^2}{2} + \alpha\|\beta\|_1\right), \quad (3)$$

where n is the number of samples, w is the weight of samples, $l(y, \eta)$ is the negative log-likelihood function, λ is the regularization parameter that controls the amount of shrinkage, α is the elastic-net penalty, and $\|\beta\|_1$ and $\|\beta\|_2$ are the L1-norm and L2-norm, respectively. When $\alpha = 0$ the estimator becomes Ridge. When $\alpha = 1$, the estimator becomes Lasso. By combining the advantages of Ridge and Lasso regression, elastic-net is capable of screening highly correlated features while ensuring the stability of the model [41].

To determine the optimal solution of α and λ, we employed the cross-validation technique. We first selected 100 groups of α values (between 0 and 1 with 0.01 increment) for a threefold cross-validation. Next, we performed another threefold cross-validation, which was repeated 10,000 times for different λ values.

2.4. Stacking Model for Multiclass Classification. The last part of our system is built on an intelligent multithreat identification model that automatically distinguishes and classifies diverse tunnel disturbances by jointly analyzing the input multidimensional features. In an attempt to create a model with good recognition performance and generalization ability, we used stacking ensemble learning [42], which is a hybrid learning strategy where multiple machine learning models are optimally combined for obtaining better classification results than any single model in the ensemble. The architecture of a stacking ensemble learning model involves a diverse range of base models and a meta model that combines the predictions of the base models. Due to the nature of stacked ensembles, it typically yields better predictive performance than individual models. In this section, we will present the framework of stacking ensemble learning, including the design of base classifiers and the meta-classifier. Performance evaluation and comparisons with individual classifiers will be provided in Section 4.4.

Figure 2 illustrates the architecture of the stacking ensemble learning model. The stacking framework has a two-level structure: the first base-classifier layer and the second meta-classifier layer. We first split the data into a training set and a test set in a 7:3 ratio. After three pieces of training, the predictions of the entire original training set were obtained. This was repeated for each base classifier to form a new training set for the meta classifier. Next, we trained the base classifiers with the original training set to obtain predictions of the test set, which were used as a new test set. Finally, the meta classifier was trained using the new training set and tested with the new test set to generate final classifications. Since the training set of the meta classifier is not involved in the training of each base classifier, overfitting can be effectively avoided. In addition, the meta classifier integrates the outputs of the base classifiers, thus improving the overall accuracy of the model.

Base-classifier design is critical to stacking ensemble learning. We compared 10 classification algorithms that cover a variety of popular methods for machine learning algorithms: SVM, XGBoost, RF, logistic regression (LR), k-nearest neighbor (KNN), multilayer perceptron (MLP), Naive Bayes (NB), long short-term memory (LSTM), probabilistic neural network (PNN), and back-propagation (BP) neural network. In order to improve the classification

schm, 2025, 1, Downloaded from https://onlinelibrary.wiley.com/doi/10.1155/stc/9780866 by Cochrane Czech Republic, Wiley Online Library on [21/03/2026]. See the Terms and Conditions (https://onlinelibrary.wiley.com/terms-and-conditions) on Wiley Online Library for rules of use; OA articles are governed by the applicable Creative Commons License

Table 1: Parameter settings of denoising algorithms.

Filter	Parameter	Explanation
CEEMD	Nstd = 0.5	Ratio of the standard deviation of added white noise to the standard deviation of raw signal
	NR = 50	Number of iterations (number of noise additions)
VMD	$K = 5$	Mode number
	Alpha = 2000	Penalty coefficient
	Tol = 1e − 6	Convergence tolerance
WTD	db3	Wavelet name
	Soft threshold	Threshold function
	Lev = 4	Decomposition level
EMD	—	A function in MATLAB without adjusting parameters

Abbreviations: CEEMD, complementary ensemble empirical mode decomposition; EMD, empirical mode decomposition; VMD, variational mode decomposition; WTD, wavelet threshold denoising.

Table 2: The 24-dimensional feature space before feature selection.

	Signal features	Abbreviation or acronym
Waveform features		
1	Mean	—
2	Peak-to-peak	P-P
3	Average rectified value[a]	ARV
4	Variance	—
5	Kurtosis[b]	—
6	Skewness[c]	—
7	Root mean square	RMS
8	Form factor[d]	FF
9	Crest factor[e]	CF
10	Impulse factor[f]	IF
11	Clearance factor[g]	CLF
Spectral features		
12	Spectral centroid frequency	SCF
13	Mean square frequency	MSF
14	Variance of normalized power spectral density (PSD)	PSD.V
15	Standard deviation of normalized PSD	PSD.SD
Spectrogram features[h]		
16	Area of binary image	Area
17	Perimeter of binary image	Perimeter
18	Compactness ratio of binary image	CR
19	Connected component of binary image	CC
20	Euler number of binary image	Eu
Spectral kurtosis features		
21	Mean of spectral kurtosis	SK.Mean
22	Standard deviation of spectral kurtosis	SK.SD
23	Skewness of spectral kurtosis	SK.skewness
24	Kurtosis of spectral kurtosis	SK.kurtosis

[a]Mean of the absolute value of the signal.
[b]Peakness of the signal.
[c]Asymmetry of a signal distribution.
[d]RMS divided by the mean of the absolute value of the signal.
[e]Peak value divided by the RMS of the signal.
[f]The height of a peak to the mean level of the signal.
[g]Peak value divided by the squared mean value of the square roots of the absolute amplitudes of the signal.
[h]Features of binary image by short-time Fourier transform.

performance of base classifiers, we employed particle swarm optimization (PSO) optimization techniques [43] to automatically tune the hyperparameters of the base models.

Four scoring metrics were employed to assess the performance of machine learning models: accuracy (A), precision (P), recall (R), and f1-score (F). The formulas for these scores are

schm, 2025, 1, Downloaded from https://onlinelibrary.wiley.com/doi/10.1155/stc/9780866 by Cochrane Czech Republic, Wiley Online Library on [21/03/2026]. See the Terms and Conditions (https://onlinelibrary.wiley.com/terms-and-conditions) on Wiley Online Library for rules of use; OA articles are governed by the applicable Creative Commons License

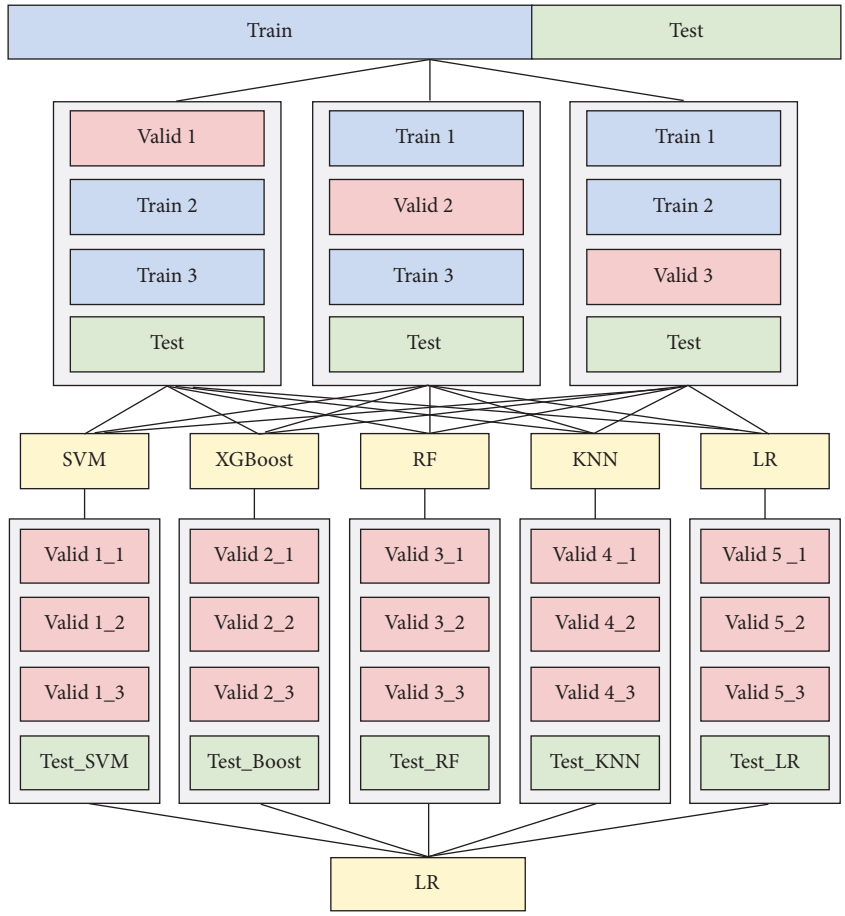

Figure 2: Architecture of the stacking ensemble learning model.

$$A = \frac{\mathrm{TP} + \mathrm{TN}}{\mathrm{TP} + \mathrm{TN} + \mathrm{FP} + \mathrm{FN}}, \tag{4}$$

$$P = \frac{\mathrm{TP}}{\mathrm{TP} + \mathrm{FP}}, \tag{5}$$

$$R = \frac{\mathrm{TP}}{\mathrm{TP} + \mathrm{FN}}, \tag{6}$$

$$F = \frac{2PR}{\mathrm{P} + \mathrm{R}}, \tag{7}$$

where TP, TN, FP, and FN are the abbreviations of true positives, true negatives, false positives, and false negatives, respectively. In addition, we used the macro-averaging method for evaluating scoring metrics for the multiclass classification problem. We first calculated P, R, and F1 according to equations (5)–(7). Then, we calculated their arithmetic means to obtain macro-precision, macro-recall, and macro-f1, respectively.

3. Data Preparation

We have developed a fiber-optic DAS dataset of tunnel disturbance events. The dataset is composed of 1,494 signals from nine types of tunnel-threatening vibration events that cover both the tunnel construction and operation periods, including excavation (174), earth boring (139), rock drilling (265), hand digging (172), water leakage (32), rockfall (167), shotcreting (166), walking (276), and train passing (103) (the sample size in each type is given in parentheses). The data were collected from various tunnels that span tunnel types, soil conditions, and geographical conditions. To avoid an unbalanced dataset that may bias the performance of our trained model, we performed simulation experiments in a real tunnel environment to increase the sample size of the rockfall category (141 out of 167 samples are from the simulations). Example waveforms and spectrograms of the nine types of events are shown in Figure 3, together with a table summarizing their durations, frequency ranges, and waveform characteristics (Table 3).

Imbalanced datasets can affect the accuracy of machine learning models, biasing toward majority categories. Generally, if the sample sizes of different categories differ by a factor of 100 or more [44], standard performance measures may not be effective and would need modification. To evaluate the appropriateness of sample size distribution in our dataset, we performed a computational experiment as follows. First, we assumed that our dataset is unbalanced and solves the problem by using a resampling strategy. Specifically, we balanced the dataset by oversampling (or undersampling) to increase (respectively, decrease) the sample size in each category while keeping the total sample

schm, 2025, 1, Downloaded from https://onlinelibrary.wiley.com/doi/10.1155/stc/9780866 by Cochrane Czech Republic, Wiley Online Library on [21/03/2026]. See the Terms and Conditions (https://onlinelibrary.wiley.com/terms-and-conditions) on Wiley Online Library for rules of use; OA articles are governed by the applicable Creative Commons License

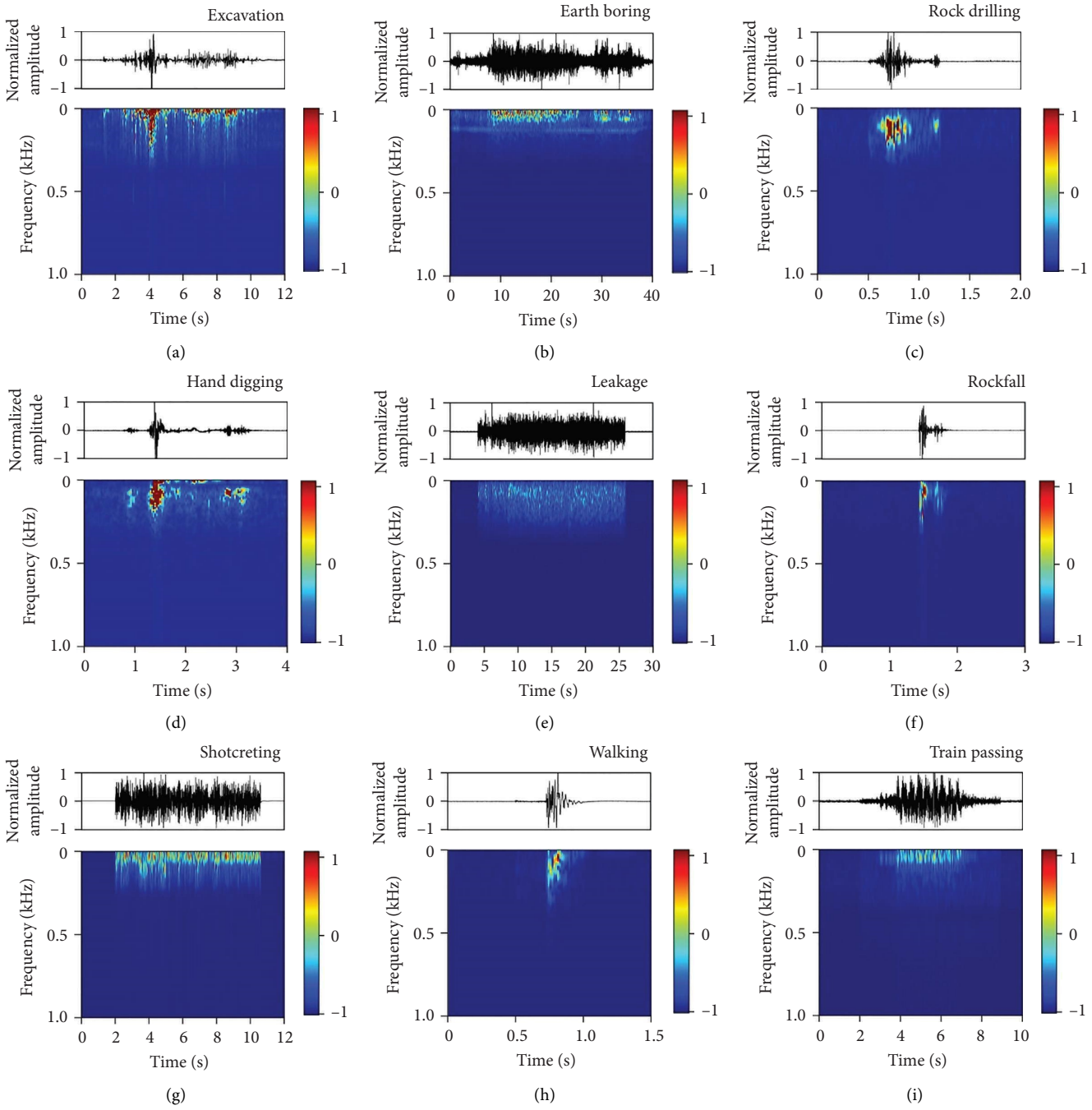

Figure 3: Waveforms and spectrograms of nine types of events: (a) excavation, (b) earth boring, (c) rock drilling, (d) hand digging, (e) water leakage, (f) rockfall, (g) shotcreting, (h) walking, and (i) train passing.

Table 3: Nine types of tunnel-threatening events detected by the intelligent DAS monitoring system.

Event	Duration (s)	Frequency (Hz)	Waveform characteristics
Ambient noise	Random	Random	Continuous with random fluctuations, weak energy
Earth boring	8.00–30.00	20–80	Continuous and stable, strong energy
Excavation	6.00–10.00	0–50	Continuous but fluctuating, strong energy
Train passing	5.00–6.00	0–120	Continuous, strong energy
Hand digging	4.00–6.00	50–200	Continuous but fluctuating, weak energy
Rockfall	0.40–0.80	0–350	Abrupt jumping, strong energy, rapid decay
Walking	0.06–0.09	0–160	Abrupt jumping, weak energy
Rock drilling	0.01–0.03	70–280	Continuous and stable, strong energy
Water leakage	—	80–350	Continuous but fluctuating, weak energy
Shotcreting	—	50–300	Continuous and stable, strong energy

schm, 2025, 1, Downloaded from https://onlinelibrary.wiley.com/doi/10.1155/stc/9780866 by Cochrane Czech Republic, Wiley Online Library on [21/03/2026]. See the Terms and Conditions (https://onlinelibrary.wiley.com/terms-and-conditions) on Wiley Online Library for rules of use; OA articles are governed by the applicable Creative Commons License

number constant (see Table 4 for the original and balanced distributions of event categories). Then, we trained three ML models on the original and resampled datasets by implementing a threefold cross-validation framework. The results show that dataset resampling had a very limited impact on the accuracy of the models, indicating that the sample size is appropriate for each type in our dataset (Table 5).

4. Results

4.1. Threshold Selection for Signal Detection. The dual thresholds of the STA/LTA ratio—which compares the average energy in an STA leading window to that in an LTA trailing window—are key to the robustness of the algorithm. To determine the base value for the upper threshold, we scrutinized the triggered STA/LTA ratio for all 1,494 samples of our dataset. The minimum ratio was set as the upper threshold, rounded down to 2.0. Based on the background noise level recorded by DAS in the Jing–Xiong intercity railway tunnel at 12:00 a.m. on July 28, 2020, UTC + 8 (details of the monitoring campaign are presented later), we chose 0.8 as the low threshold and a 5-second background noise as the standard noise. To extract the detected signals from the ambient vibration recordings while discarding unwanted data, we used the normalized cumulative energy curve, which allowed us to separate the signals of interest from the background noise in real time (Figure 4). Nine different types of tunnel disturbances captured by the anomaly detection pipeline are depicted in Figure 5, showing that even very low amplitude signals can be successfully detected.

4.2. Top Denoiser Evaluation. The side-to-side comparison of four denoisers (Figure 6) showed that CEEMD performed better overall in terms of SNR and RMSE, followed closely by VMD. For smoothness, EMD was superior to the other methods. VMD and WTD did not perform particularly well as expected. VMD, as the name implies, depends heavily on parameter tuning, especially the number of intrinsic mode functions, which varies with events. However, the mode number had to be fixed in the system (four, determined by a trial-and-error procedure), which caused under- or over-decomposition of certain types of signals, thus reducing the overall denoising performance. For WTD, the selection of wavelet function is an important factor affecting the algorithm performance. Here, we adopted a common parameter configuration of WTD: Daubechies extremal phase wavelets (db3), soft threshold, and four-level decomposition. Although a four-level wavelet decomposition can easily distinguish sharp signals from noise (e.g., rockfalls and walking), the small vanishing moment of db3 could make the signal unsmooth, leading to some loss of frequency-domain details, which explains WTD's relatively poor smoothness metrics in some event categories.

Based on the above performance evaluation, we excluded WTD because of its poor performance on all three metrics and EMD as it improves the smoothness by severely compromising SNR. Both CEEMD and VMD have excellent generalization capability, but the former can achieve relatively better denoising while requiring less computation time. Therefore, we finally chose CEEMD as the top denoising method for the nine tunnel anomalous signals. In addition, our results suggest that the number of tunable parameters plays a particularly important role when selecting a denoising method for multiclass vibration signals. Filters with fewer parameters usually have stronger transfer ability and therefore perform better overall on multiclass signals. In contrast, filters that rely extensively on parameter adjustment, such as VMD and WTD, are better suited for denoising specific vibration events.

Table 4: Original and balanced distributions of event categories.

Event category	Original	Resampled
Excavation	174	166
Earth boring	139	166
Rock drilling	265	166
Hand digging	172	166
Water leakage	32	166
Rockfall	167	166
Shotcreting	166	166
Walking	276	166
Train passing	103	166

4.3. Common Feature Set. We first examined the relative importance of the 24 features for event recognition using elastic-net regression. To avert inflated performance evaluations due to overfitting, we split our dataset into a training set and a test set using a 7:3 ratio. Briefly, a threefold cross-validation procedure was used to determine the best values of two key elastic-net model parameters (alpha = 0.2, lambda = 0.00043) (Methods). Figure 7(a) shows how the regression coefficients calculated by elastic-net dynamically shrink with lambda; each line indicates the shrink trend of the coefficient of a specific feature. We graphed a feature importance chart according to the regression coefficients at the optimal lambda value 0.00043 (Figure 7(b)). We find that the total importance of the waveform and spectral features reached 75.29% (45.17% + 30.12%), indicating that the differences between the various types of tunnel vibration signals are mainly in their time- and frequency-domain features.

The most important feature for classification is crest factor (11.24%), a metric with high separation ability for impulsive signals (i.e., signals of large magnitude that occur over a short time interval). Interestingly, in the second and third places are both variance-related features: variance of normalized power spectral density (11.08%) and variance of wave amplitude (8.31%). Variance is a statistical measure of how discrete data points differ from the mean. The fact that two of the top three features are associated with variance indicates that our elastic-net model found signal variability to be the most useful in differentiating between different events. The importance of spectrogram and spectral kurtosis features is relatively low, accounting for 12.02% and 12.69%, respectively. They were included in the feature vector to enrich the variety of feature categories and improve the predictive power.

schm, 2025, 1, Downloaded from https://onlinelibrary.wiley.com/doi/10.1155/stc/9780866 by Cochrane Czech Republic, Wiley Online Library on [21/03/2026]. See the Terms and Conditions (https://onlinelibrary.wiley.com/terms-and-conditions) on Wiley Online Library for rules of use; OA articles are governed by the applicable Creative Commons License

Table 5: Performance metrics of models on original and balanced datasets.

Model	Metric	Score (original dataset) (%)	Score (balanced dataset) (%)
SVM	Accuracy	96.44	96.65
	Precision	96.70	96.68
	Recall	95.68	95.73
	F1-score	96.15	95.78
RF	Accuracy	93.76	94.10
	Precision	94.08	94.49
	Recall	93.48	93.67
	F1-score	93.70	94.08
XGBoost	Accuracy	95.99	95.54
	Precision	96.21	96.01
	Recall	95.04	95.24
	F1-score	95.56	95.56

Abbreviations: RF, random forest; SVM, support vector machine; XGBoost, eXtreme gradient boosting.

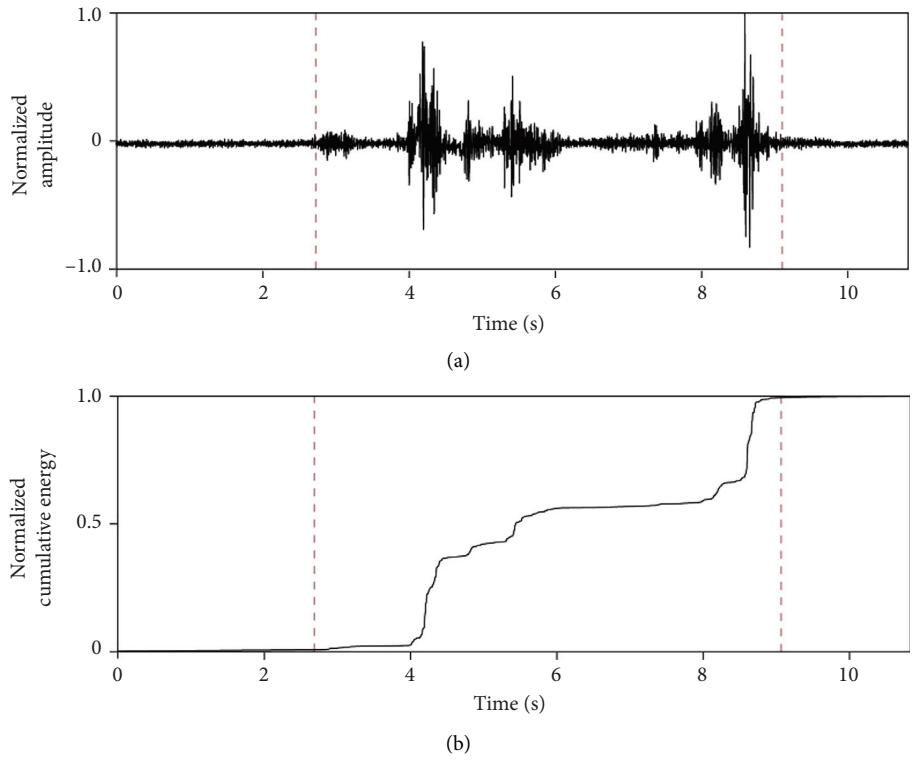

Figure 4: Example Husid plot of tunnel disturbance signal. (a) An excavation event signal from distributed acoustic sensing recordings. (b) The normalized cumulative energy curve. Vertical lines indicate the times at which the cumulative integral of amplitude squared reaches 0.5% and 99.5% of the maximum value.

Multicollinearity among independent variables can lead to unreliable predictions [41]. To avoid collinearity and reduce the dimensionality of our feature space, we combined heatmap correlation analysis with the feature importance to filter out features that are statistically highly intercorrelated and of relatively low importance for recognition. According to the feature-correlation heatmap (Figure 7(c)), skewness was excluded because it is highly correlated with area ($r = 0.97$), clearance factor ($r = 0.97$), and crest factor ($r = 0.93$). Clearance factor has a high correlation of $r > 0.9$ with crest factor or impulse factor, and all three features are sensitive to impulsive signals, so we removed clearance factor to reduce multicollinearity. The average rectified value is linearly correlated with impulse factor ($r = 1$); we retained the latter for its slightly higher importance score. Variance, form factor, and kurtosis are three highly intercorrelated features; we kept only variance to optimize the feature space. Because mean had little importance for classification (0.1%), it was removed to reduce computational efforts. In total, we selected five waveform features. Likewise, multicollinearity

schm, 2025, 1, Downloaded from https://onlinelibrary.wiley.com/doi/10.1155/stc/9780866 by Cochrane Czech Republic, Wiley Online Library on [21/03/2026]. See the Terms and Conditions (https://onlinelibrary.wiley.com/terms-and-conditions) on Wiley Online Library for rules of use; OA articles are governed by the applicable Creative Commons License

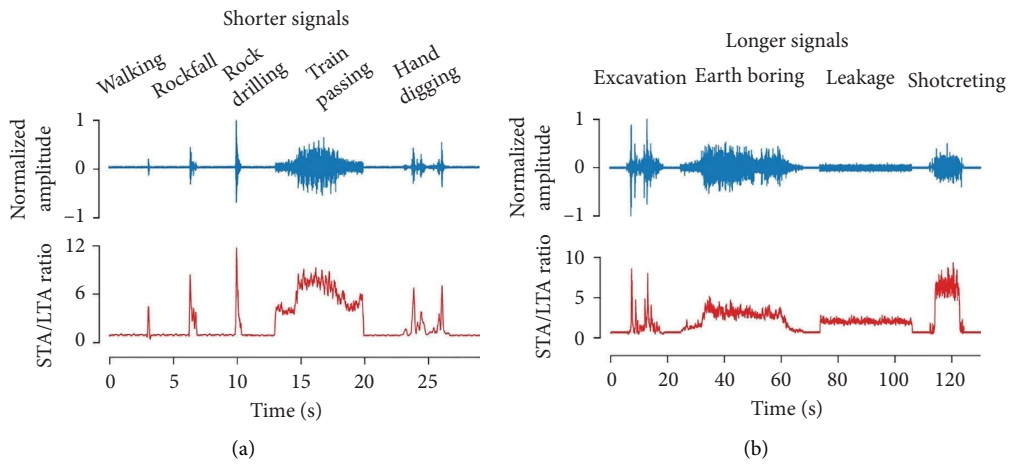

Figure 5: Example time-series waveforms and the corresponding STA/LTA ratios of nine types of tunnel disturbance events obtained with our anomaly detection subsystem. (a) Left, shorter signals. (b) Right, longer signals.

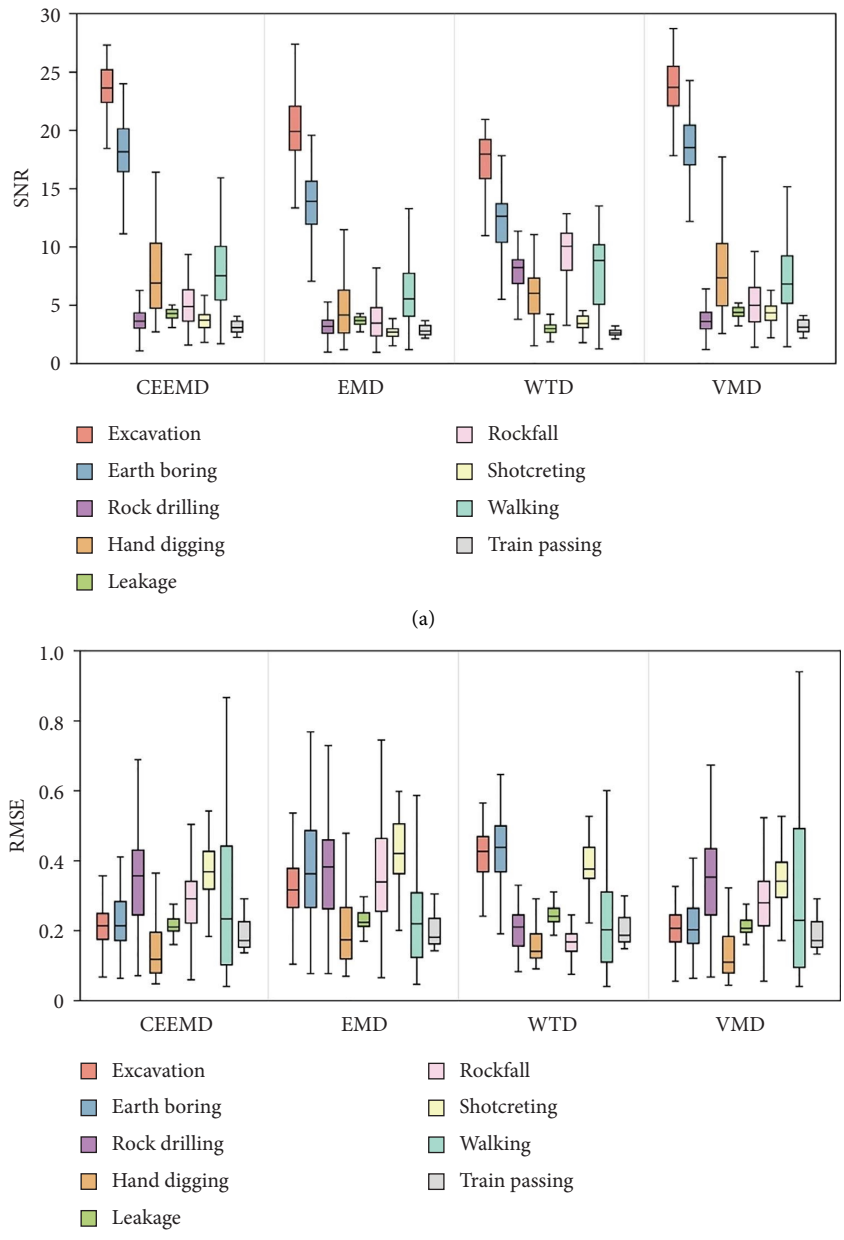

Figure 6: Continued.

schm, 2025, 1, Downloaded from https://onlinelibrary.wiley.com/doi/10.1155/stc/9780866 by Cochrane Czech Republic, Wiley Online Library on [21/03/2026]. See the Terms and Conditions (https://onlinelibrary.wiley.com/terms-and-conditions) on Wiley Online Library for rules of use; OA articles are governed by the applicable Creative Commons License

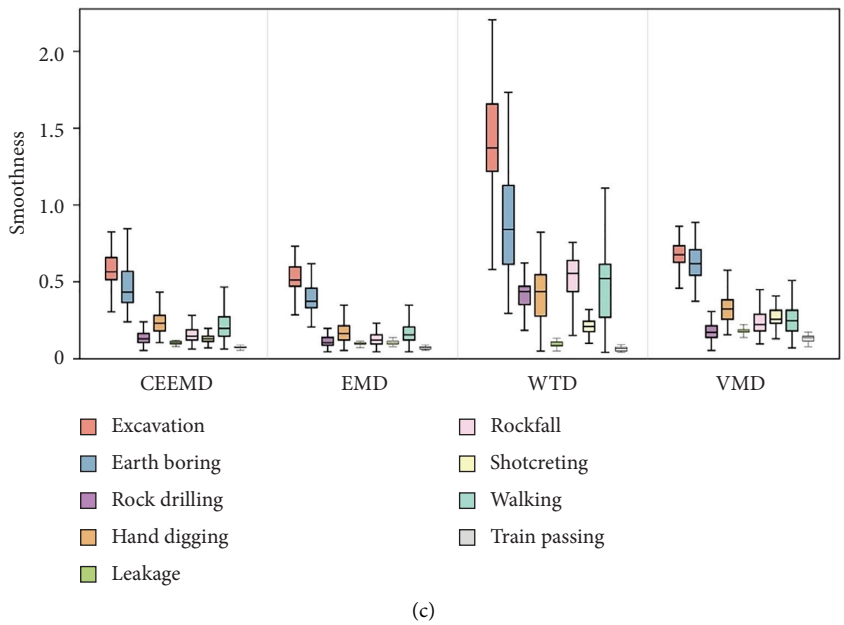

(c)

Figure 6: Denoising performance comparison. (a) SNR. (b) RMSE. (c) Smoothness.

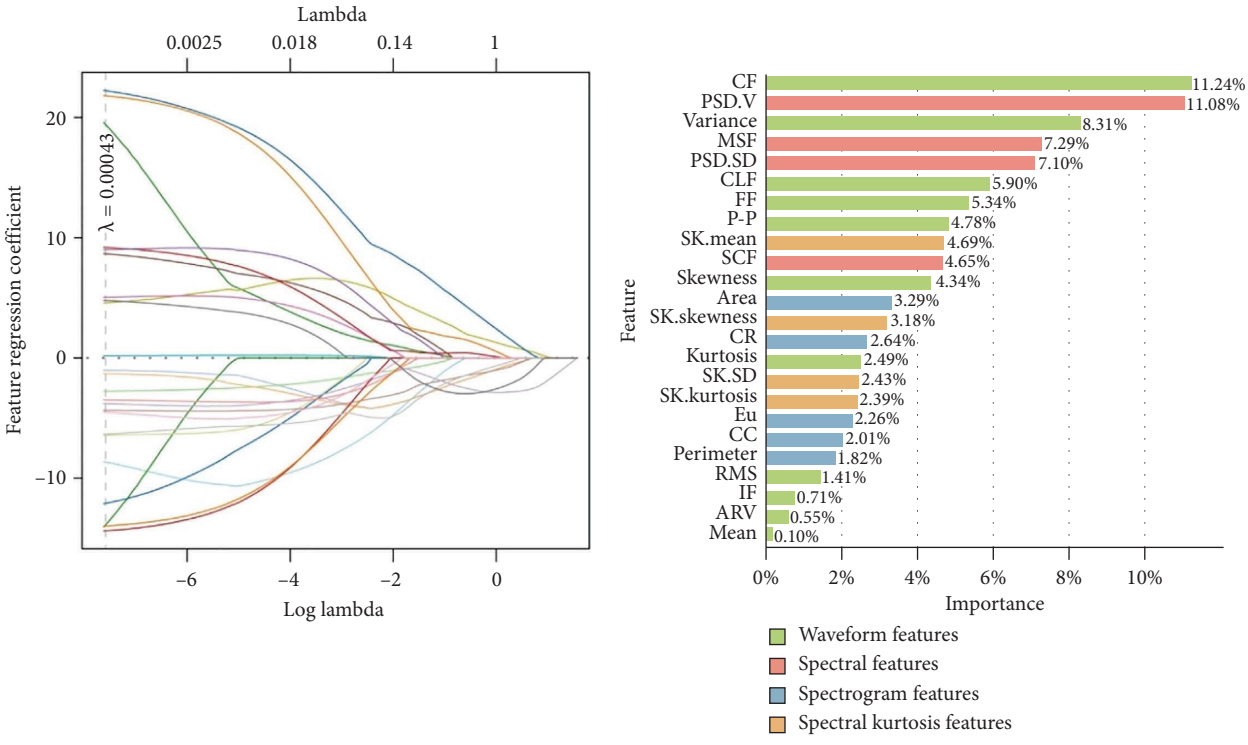

(a) (b)

Figure 7: Continued.

schm, 2025, 1, Downloaded from https://onlinelibrary.wiley.com/doi/10.1155/stc/9780866 by Cochrane Czech Republic, Wiley Online Library on [21/03/2026]. See the Terms and Conditions (https://onlinelibrary.wiley.com/terms-and-conditions) on Wiley Online Library for rules of use; OA articles are governed by the applicable Creative Commons License

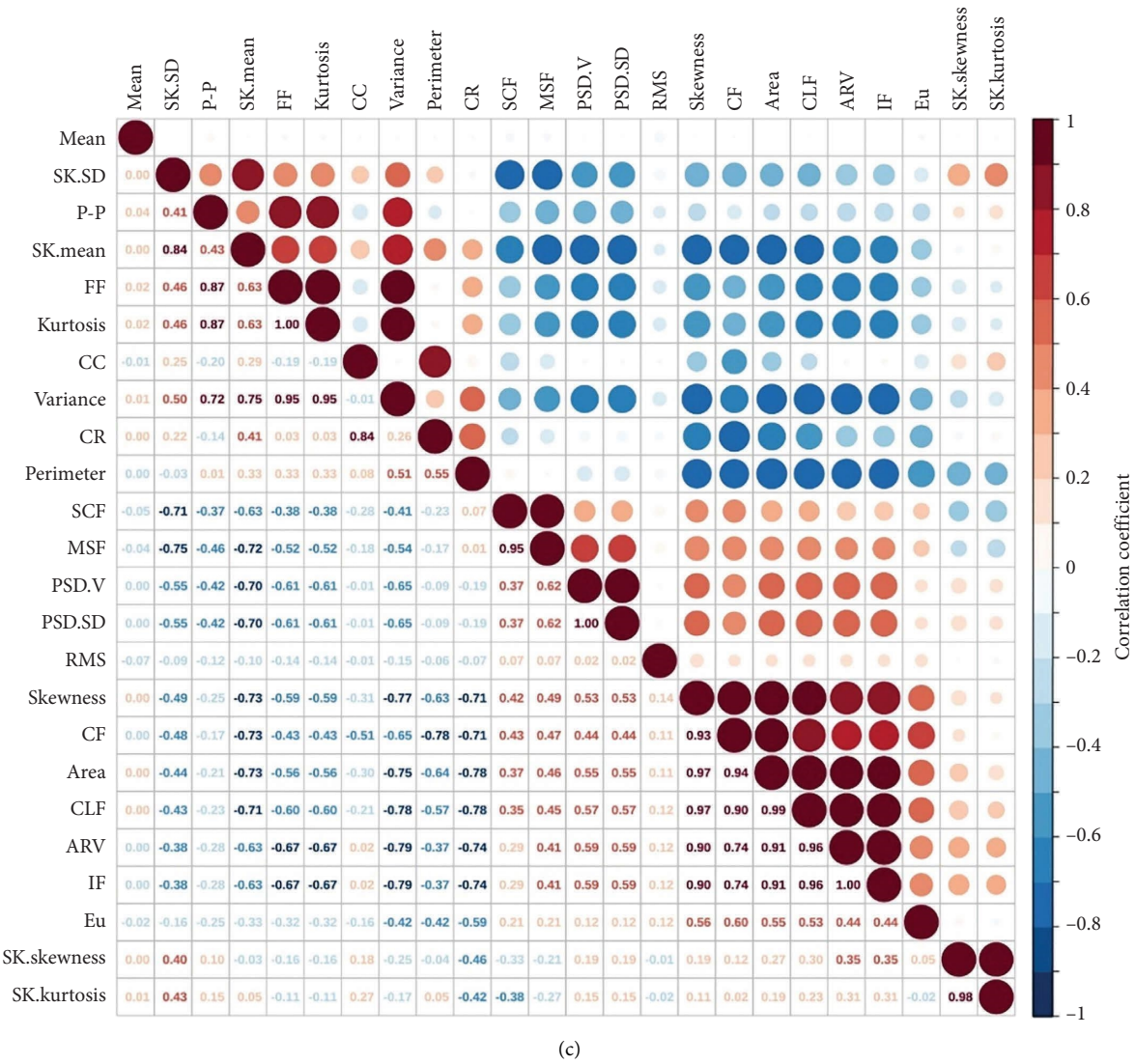

(c)

FIGURE 7: Feature selection. (a) Elastic-net variable trace profiles of 24 signal features. The dashed line indicates the best lambda value 0.00043 determined by a threefold cross-validation. (b) Feature importance with best lambda value 0.00043. (c) Heatmap of Pearson correlation coefficients of the features.

correction and dimensionality reduction were performed for the other three feature categories considering both feature correlation and feature importance. Combining heatmap correlation analysis and elastic-net regression, we removed nine features with statistically high intercorrelation or of relatively low importance, leaving 15 predictive features (features 2, 4, 7, 9, 10, 12, 14, 16–20, and 21–23 in Table 2) for downstream machine learning and pattern recognition. For each detected signal, our feature extraction module generates a vector containing 15 feature values for downstream pattern recognition.

To illustrate how dimensionality reduction quantitatively improves the recognition ability of our final stack model, we used the dataset of 24 and 15 features, respectively, to train the model using a threefold cross-validation, optimized with PSO. The results show that feature selection improves the accuracy, precision, recall, and F1-score by 1.34%, 1.70%, 0.71%, and 1.21%, respectively (Figure 8).

4.4. Multiclass Classification Results

4.4.1. Base Classifier Selection. We compared 10 classification algorithms that cover a variety of popular methods for machine learning. According to the algorithm principle, LSTM is a deep learning method with some memory effect and is suitable for processing time-series data with massive variables. We excluded LSTM because it is poorly interpretable with many tunable parameters, which was considered unsuitable for the current supervised multiclassification task. We removed the PNN and BP algorithms because they have been incorporated into other algorithms as basic methods. For example, the gradient transfer method in the MLP algorithm is based on the idea of BP.

We evaluated the remaining seven classifiers on a performance basis. A threefold cross-validation framework was implemented, and PSO was used for optimization (Table 6). According to a side-to-side performance comparison as well

schm, 2025, 1, Downloaded from https://onlinelibrary.wiley.com/doi/10.1155/ste/9780866 by Cochrane Czech Republic, Wiley Online Library on [21/03/2026]. See the Terms and Conditions (https://onlinelibrary.wiley.com/terms-and-conditions) on Wiley Online Library for rules of use; OA articles are governed by the applicable Creative Commons License

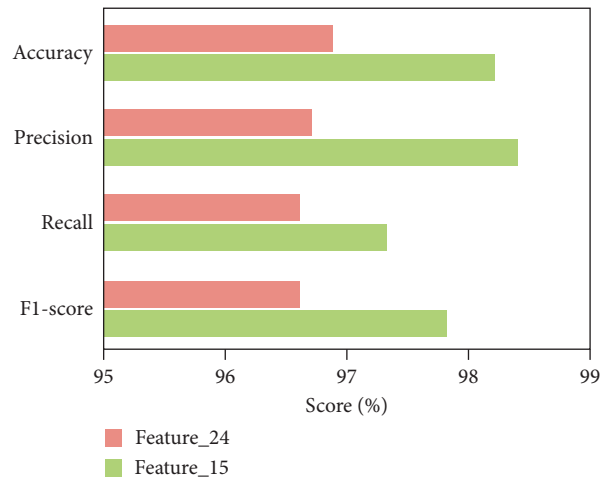

Figure 8: Effect of feature reduction on the performance of the stacking model.

Table 6: Hyperparameter settings of base classifiers.

Base classifier	Hyperparameter	Explanation
SVM	$C = 22.4690$ Gramma = 5.9034	Coefficients of the L2-norm Kernel coefficient
LR	$C = 50$	Reciprocal of the coefficients of L2-norm
KNN	n_neighbors = 3	Number of neighbors (K value in KNN)
MLP	hidden_layer_sizes = 50 Alpha = 0.1	Number of neurons in the hidden layer Coefficients of the L2-norm
NB	var_smoothing = 1.00E − 06	Portion of the largest variance of all features
RF	n_estimators = 70 max_depth = 10	Number of decision trees Maximum depth of decision tree
XGBoost	n_estimators = 100 max_depth = 3	Number of decision trees Maximum depth of decision tree

Abbreviations: KNN, k-nearest neighbor; LR, logistic regression; MLP, multilayer perceptron; NB, Naive Bayes; RF, random forest; SVM, support vector machine; XGBoost, eXtreme gradient boosting.

Table 7: Performance of seven classifiers on tunnel disturbance event classification.

Model	Accuracy (%)	Precision (%)	Recall (%)	F1-score (%)
SVM	96.44	96.70	95.68	96.15
LR	94.43	93.18	94.64	93.74
KNN	94.21	95.04	93.34	93.99
MLP	89.98	86.80	88.62	87.38
NB	87.31	85.57	88.49	85.56
RF	93.76	94.08	93.48	93.70
XGBoost	95.99	96.21	95.04	95.56

Abbreviations: KNN, k-nearest neighbor; LR, logistic regression; MLP, multilayer perceptron; NB, Naive Bayes; RF, random forest; SVM, support vector machine; XGBoost, eXtreme gradient boosting.

as considering their algorithmic characteristics (Table 7), we selected five well-performing models as our base classifiers: SVM, XGBoost, RF, LR, and KNN. We chose LR as our meta classifier to combine the predictions from the base classifiers.

4.4.2. Stacking Model Performance Evaluation. To examine whether stacking improved the classification ability of the machine learning model, we benchmarked the performance of our model against two other ensemble strategies: boosting and bagging. We built three stacking models: stacking_E1 is our final model with SVM, XGBoost, RF, LR, and KNN as the base classifiers; stacking_E2 is essentially stacking_E1 plus MLP and NB; and stacking_E3 removes XGBoost and RF from stacking_E2. LR is the meta classifier for all three stacking models. Again, we implemented a threefold cross-validation framework with hyperparameter tuning using PSO. We graphed the evaluation results by algorithm type (Figure 9(a)) and event category (Figure 9(b)). For simplicity, we used Categories 1–9 to represent, in order,

schm, 2025, 1, Downloaded from https://onlinelibrary.wiley.com/doi/10.1155/ste/9780866 by Cochrane Czech Republic, Wiley Online Library on [21/03/2026]. See the Terms and Conditions (https://onlinelibrary.wiley.com/terms-and-conditions) on Wiley Online Library for rules of use; OA articles are governed by the applicable Creative Commons License

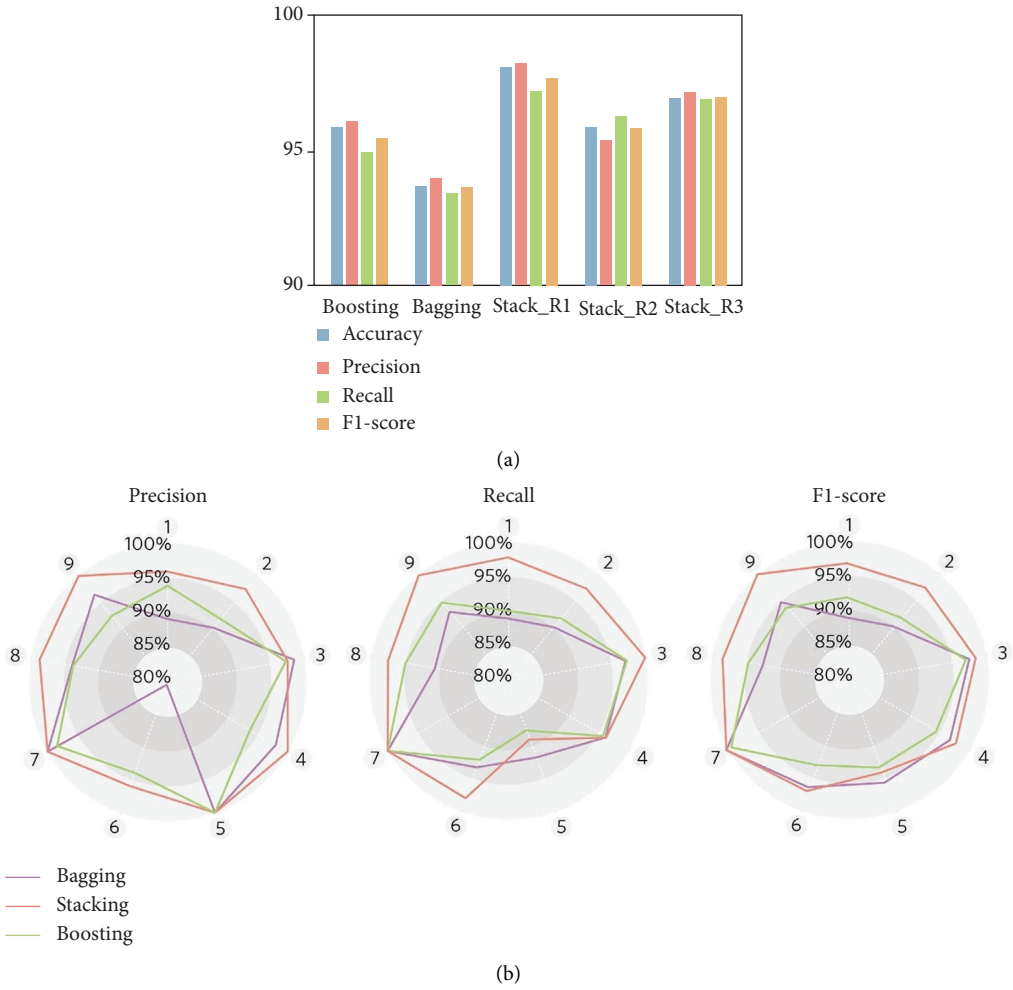

FIGURE 9: System performance. (a) Performance comparison between ensemble learning models. (b) Performance of ensemble models on nine individual tunnel disturbance events.

excavation, earth boring, rock drilling, hand digging, water leakage, rockfall, shotcreting, walking, and train passing.

The comparison with the test set demonstrated that our stacking model (stacking_E1) had better overall (macro) performance than boosting, bagging, and the other two stacking models in classifying various tunnel disturbances (Figure 9(a)). For example, our stacking model had a macro-accuracy of 98.22%, which was 2.23% higher than boosting and 4.46% higher than bagging. With five good classifiers in the ensemble, stacking_E1 achieved a 1.12% higher accuracy than stacking_E3. In addition, increasing the number of base classifiers does not necessarily improve the model's recognition ability. For example, stacking_E1 with only five classifiers outperformed stacking_E2 with seven classifiers due to the poor performance of the added MLP and NB. This emphasizes the importance of base-classifier selection for ensemble learning models.

This evaluation also showed that stacking_E1 scored higher on almost all individual event categories than other models (Figure 9(b)). Our trained model was the most precise in recognizing eight event categories except for rock drilling (Category 3), on which it scored 97.59%, only 0.96% less precise than bagging. In terms of recall and F1-score, our model scored lower than bagging only in water leakage (Category 5), with a difference of 2.78% (recall) and 1.53% (f1-score), respectively.

Of the eight event categories, rockfall (Category 6) is not only among the most crucial monitoring target from a geotechnical perspective but also the least reliably identified. Our model recognized rockfall with an F1-score of 96.91% (the second lowest F1-score), compared to 100% for shotcreting (Category 7) and train passing (Category 9). This low F1-score is mainly due to the high overlap of the spectral kurtosis feature SK.SD (sensitive to impulsive signals) between rockfall and walking (Category 8) (Figure 10(a)), both characterized by short-duration impulsive attributes. Another observation is that excavation was identified with an equally low F1-score (96.91%). This is because the excavation signal closely resembles the earth boring signal (Category 2) in the time–frequency domain binary image, leading to an overlap of the features Eu and CR describing the outline of the binary image (Figure 10(b)), which is likely to cause misclassifications.

In summary, this side-to-side comparison proves the ability of the trained stacking ensemble learning model to

schm, 2025, 1, Downloaded from https://onlinelibrary.wiley.com/doi/10.1155/stc/9780866 by Cochrane Czech Republic, Wiley Online Library on [21/03/2026]. See the Terms and Conditions (https://onlinelibrary.wiley.com/terms-and-conditions) on Wiley Online Library for rules of use; OA articles are governed by the applicable Creative Commons License

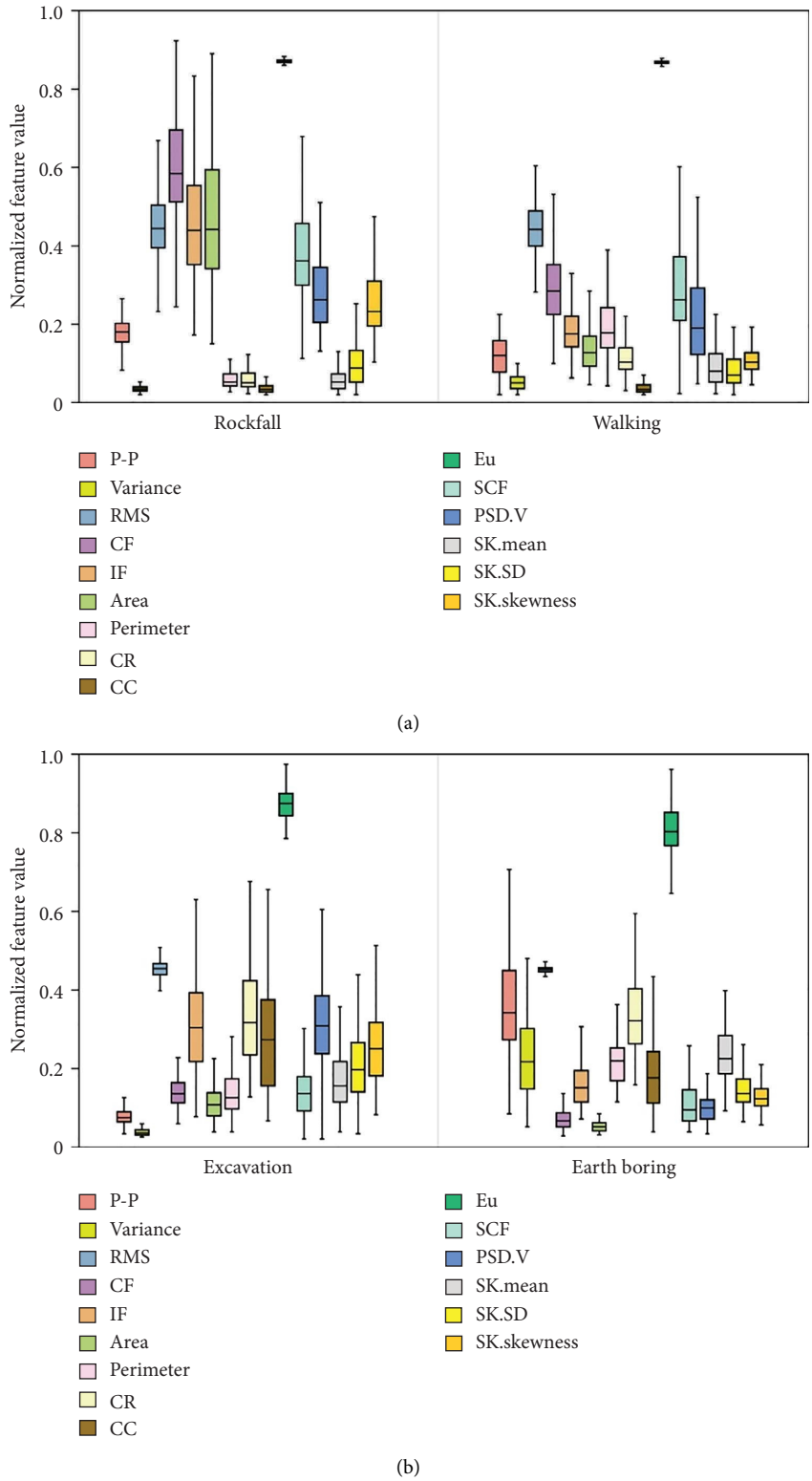

FIGURE 10: Comparison of feature values between events. (a) Rockfall and walking. (b) Excavation and earth boring. See Table 2 for explanations of the features.

schm, 2025, 1, Downloaded from https://onlinelibrary.wiley.com/doi/10.1155/stc/9780866 by Cochrane Czech Republic, Wiley Online Library on [21/03/2026]. See the Terms and Conditions (https://onlinelibrary.wiley.com/terms-and-conditions) on Wiley Online Library for rules of use; OA articles are governed by the applicable Creative Commons License

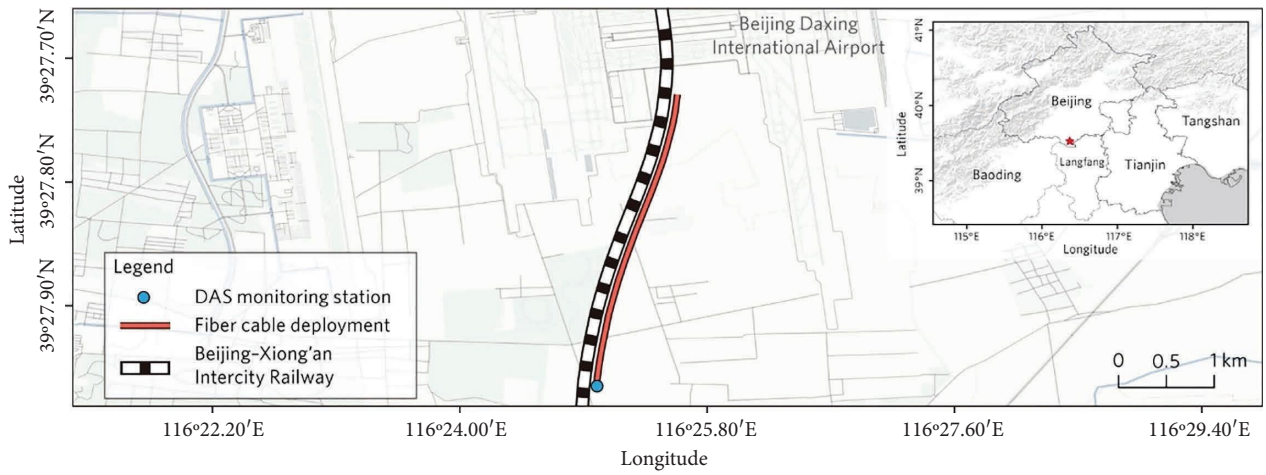

FIGURE 11: Map of optical fiber path used or DAS (red line) located in Lang fang, Hebei Province (inset, red pentagram).

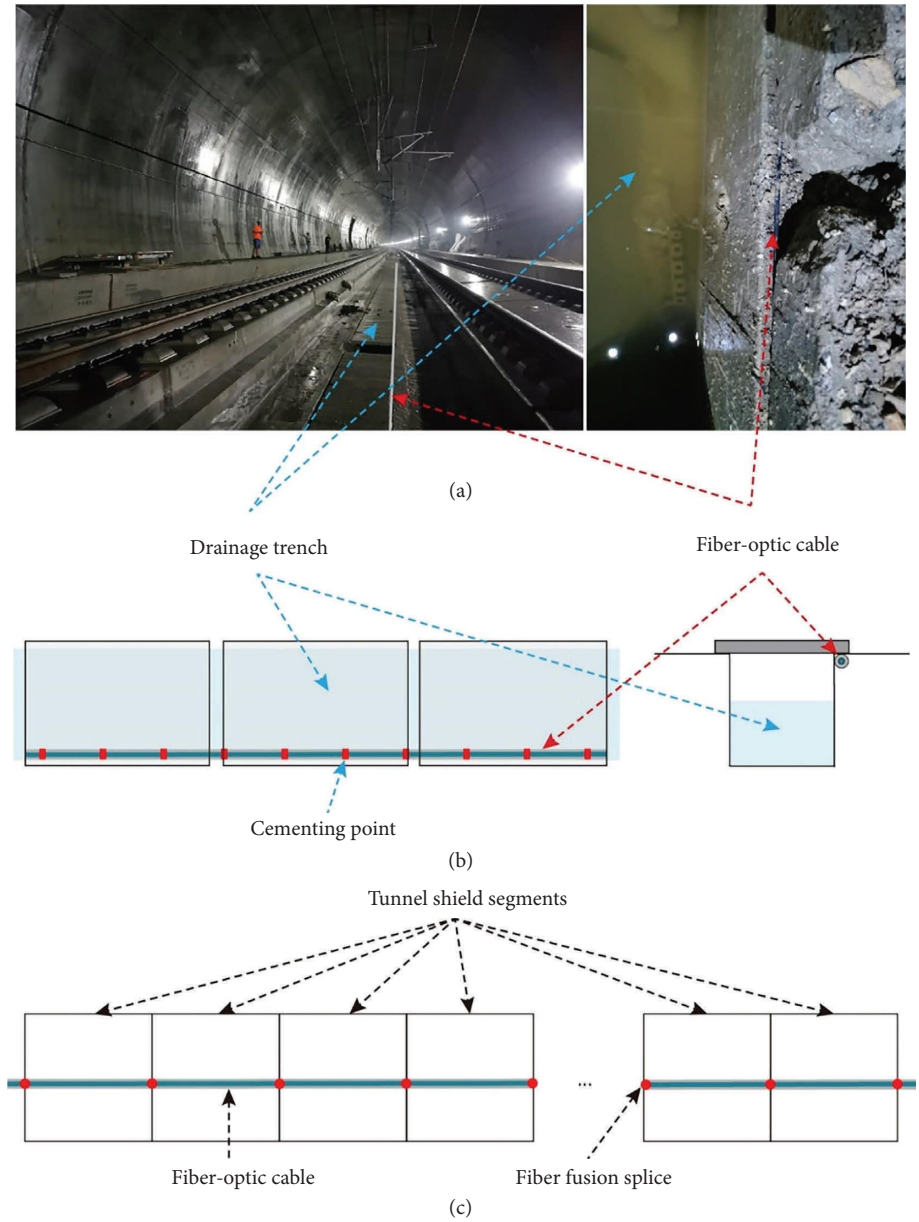

FIGURE 12: The Beijing–Xiong'an intercity railway tunnel and sensing fiber deployment scheme. (a) Photograph of the test tunnel and a close-up view of the drainage trench. (b) Layout of the fiber-optic cable near the central drainage trench. (c) Layout of the cable on the roof of the tunnel.

schm, 2025, 1, Downloaded from https://onlinelibrary.wiley.com/doi/10.1155/stc/9780866 by Cochrane Czech Republic, Wiley Online Library on [21/03/2026]. See the Terms and Conditions (https://onlinelibrary.wiley.com/terms-and-conditions) on Wiley Online Library for rules of use; OA articles are governed by the applicable Creative Commons License

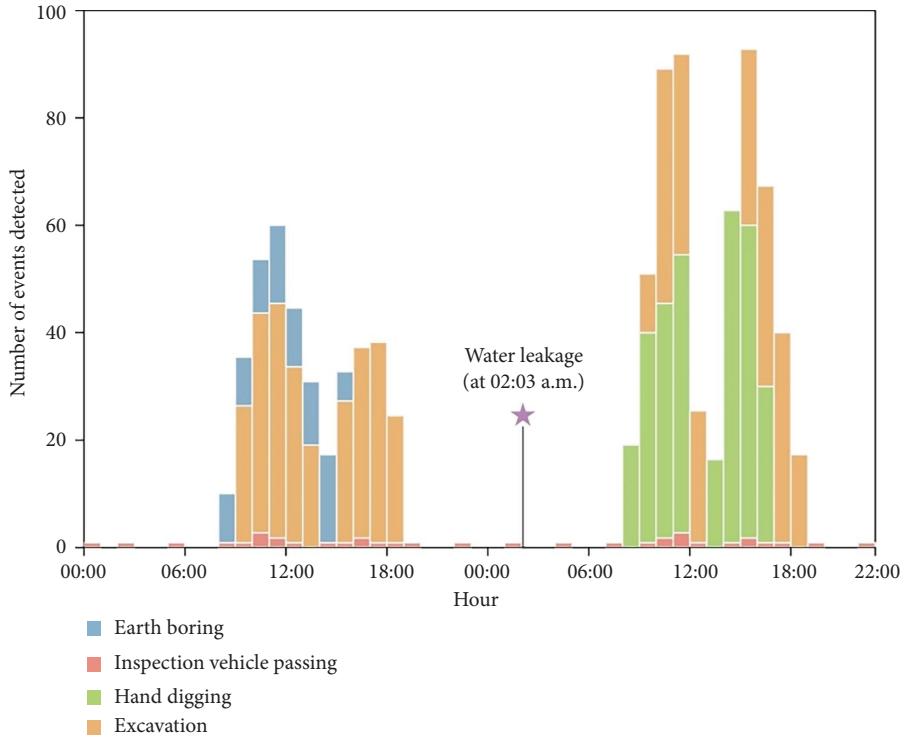

Figure 13: Disturbance events identified in the Beijing–Xiong'an intercity railway tunnel.

Figure 14: Water leakage in the tunnel.

correctly recognize multiple tunnel disturbances and also supports that stacking can harness the capabilities of sub-models on classification tasks.

5. Real-World Application

In order to verify the efficacy and transferability of our tunnel threat monitoring system, we carried out a 1-month DAS monitoring experiment at the Jing–Xiong intercity railway tunnel (Gu'an County, Hebei Province, China) (Figure 11). The test tunnel is a single-hole, double-line tunnel with a full length of 7208 m, a width of 15 m, a shallow depth of 8 m, and a maximum depth of 22 m (Figure 12). We deployed a 2-mm diameter single-mode fiber-optic cable (tight-buffered, thermoplastic polyurethane-jacketed) with a total length of 8000 m in this tunnel, which can be roughly divided into two sections. The first 4530 m of the cable was laid near the central water ditch at the bottom of the tunnel to monitor events such as rockfalls, machinery operations, and train passing. The rest of the cable were laid on top of the tunnel for intrusion and water leakage detection. The coupling between the fiber and the surrounding medium is a key factor for the successful fiber-optic monitoring [45, 46]. To ensure optimal tunnel-to-fiber coupling, we directly embedded the pretensioned cable into the groove on the sidewall of the ditch and then fixed it with epoxy resin adhesive every 1 m (Figure 12(b)). For the tunnel roof section, the surface-bonding method was used to fasten the

schm, 2025, 1, Downloaded from https://onlinelibrary.wiley.com/doi/10.1155/ste/9780866 by Cochrane Czech Republic, Wiley Online Library on [21/03/2026]. See the Terms and Conditions (https://onlinelibrary.wiley.com/terms-and-conditions) on Wiley Online Library for rules of use; OA articles are governed by the applicable Creative Commons License

cable to the tunnel segments (Figure 12(c)). Finally, the roof cable section and the ground cable section were fused at one end of the cable, while the other end was connected to a DAS integration unit (IU). Continuous vibration measurements were made by the DAS IU at a 2000-Hz sample rate with a 10-m channel spacing from August 1, 2020, to August 31, 2020, UTC + 8.

Figure 13 shows the disturbance events detected by DAS on August 29 and 30. During the 2-day monitoring period, our intelligent DAS system identified a range of tunnel disturbances, including excavation, earth boring, and inspection vehicle passing. Furthermore, the number of events recognized was highly consistent with the manual inspection record on site. In addition, our monitoring system successfully captured a small-scale water leakage event in the early morning (2:03 a.m.) of August 29. Manual inspection confirmed that it was caused by cracking of the concrete tunnel lining (Figure 14), which, if not detected in time, might develop into a larger-scale water inflow.

6. Discussion and Conclusions

We have shown how machine learning methods can be paired with the emerging DAS technology to automatically identify a variety of anomalous vibration events that threaten underground tunnels. Through a real-world application in the Jing–Xiong railway tunnel, we demonstrate how such automated monitoring enables the timely detection of weak-energy but highly dangerous events, such as water leaks. In contrast to traditional node-based microseismic monitoring methods that typically deal with specific tunnel hazards (e.g., rock bursts [47]), our intelligent surveillance system leverages the long-range sensing capability, dense spatial sampling strength, and broadband nature of DAS, thus being able to extend over tens of kilometers and detect a wide range of tunnel threats. Our stacking ensemble model integrates multiple classifiers for automatic feature learning, improving adaptability, robustness, and detection accuracy in diverse tunnel disturbance events. Furthermore, the sensing fibers—slender yet robust—can be easily deployed in confined spaces and are highly durable in subsurface environments, allowing for long-term tunnel safety monitoring. Additionally, passing trains are potential sources of vibration. With ambient noise tomography techniques [48], the passively recorded multichannel background noise can be exploited to image high-resolution stratigraphic structures around tunnels. Together, these could open up new possibilities for tunnel and underground space research.

Our work also represents an important step forward in the development of a general framework for processing and efficiently exploring sizable volumes of engineering DAS data. Several artificial intelligence–based approaches [25–29] using site-specific DAS datasets have been proved to achieve high local accuracy, but they lack transferability between sites. By contrast, the current machine learning model is highly transferable thanks to the good generalization ability of stacking ensemble learning, and most importantly, it has been trained with high-quality vibroacoustic data collected in real tunnel environments that span tunnel types, soil conditions, and geographical conditions. Moreover, selected from 24 typical signal features, our 15-dimensional feature set is exceptionally descriptive across diverse tunnel disturbances—from geologic hazards such as rockfalls and groundwater inflows to machinery operations and regular train passing. In addition, the remarkable efficacy of the automatic anomaly detection pipeline provides a universal solution for picking, separating, and denoising anomalous signals. Hence, our machine learning–based autonomous DAS monitoring approach is highly generalizable and can be well transferred to new and vastly differing tunnel environments. However, we recognize that the performance of our model could be limited by the diversity of event types in the training data. When event types not included in the training set occur, the detection accuracy may decrease significantly due to the model's difficulty in interpreting unfamiliar patterns. Therefore, our next work is to improve the model's adaptability to unknown events by employing advanced open-set algorithms and increasing the volume of training data. As more datasets become available, we anticipate that the intelligent DAS monitoring system will be able to be refined and deployed in a wide variety of underground spaces.

Data Availability Statement

The data that support the findings of this study are available from the corresponding author upon reasonable request.

Conflicts of Interest

The authors declare no conflicts of interest.

Funding

This work was supported by the National Natural Science Foundation of China grants (grant numbers 42030701 and 42107153), the Natural Science Foundation of Jiangsu Province grant (grant number BK20200217), and the Yuxiu Young Scholars Program of Nanjing University (grant number 2010619).

Acknowledgments

We are grateful to Jun Yin, Zheng Wang, Jun-Peng Li, and NanZee staff for contribution to the development of the dataset and for assistance in the field monitoring campaign. We thank Dechuan Zhan and Su Lu for advice on building the machine learning model and Zheng Wang for assistance in drawing Figure 11.

References

[1] R. K. Goel, B. Singh, and J. Zhao, *Underground Infrastructures: Planning, Design, and Construction* (Amsterdam: Elsevier, 2012).

[2] K. Soga and J. Schooling, "Infrastructure Sensing," *Interface Focus* 6, no. 4 (2016): 20160023, https://doi.org/10.1098/rsfs.2016.0023.

[3] A. Baghbani, T. Choudhury, S. Costa, and J. Reiner, "Application of Artificial Intelligence in Geotechnical

schm, 2025, 1, Downloaded from https://onlinelibrary.wiley.com/doi/10.1155/stc/9780866 by Cochrane Czech Republic, Wiley Online Library on [21/03/2026]. See the Terms and Conditions (https://onlinelibrary.wiley.com/terms-and-conditions) on Wiley Online Library for rules of use; OA articles are governed by the applicable Creative Commons License

Engineering: A State-Of-The-Art Review," *Earth-Science Reviews* 228 (2022): https://doi.org/10.1016/j.earscirev.2022.103991.

[4] R. C. Trautz and J. S. Y. Wang, "Seepage into an Underground Opening Constructed in Unsaturated Fractured Rock under Evaporative Conditions," *Water Resources Research* 38, no. 10 (2002): 6-1-6–14, https://doi.org/10.1029/2001wr000690.

[5] S. Li, B. Liu, X. Xu, et al., "An Overview of Ahead Geological Prospecting in Tunneling," *Tunnelling and Underground Space Technology* 63 (2017): 69–94, https://doi.org/10.1016/j.tust.2016.12.011.

[6] X. Wang, M. Wang, R. Jiang, et al., "Structural Deformation Monitoring during Tunnel Construction: A Review," *Journal of Civil Structural Health Monitoring* 14, no. 3 (2024): 591–613, https://doi.org/10.1007/s13349-023-00741-1.

[7] D. Anikiev, C. Birnie, U. Waheed, et al., "Machine Learning in Microseismic Monitoring," *Earth-Science Reviews* 239 (2023): https://doi.org/10.1016/j.earscirev.2023.104371.

[8] Y. Yao, S.-T. E. Tung, and B. Glisic, "Crack Detection and Characterization Techniques-An Overview," *Structural Control and Health Monitoring* 21, no. 12 (2014): 1387–1413, https://doi.org/10.1002/stc.1655.

[9] F. He, J. Chen, C. Li, and F. Xiong, "Temperature Tracer Method in Structural Health Monitoring: A Review," *Measurement* 200 (2022): https://doi.org/10.1016/j.measurement.2022.111608.

[10] V. B. Sharma, S. Tewari, S. Biswas, and A. Sharma, "A Comprehensive Study of Techniques Utilized for Structural Health Monitoring of Oil and Gas Pipelines," *Structural Health Monitoring* 23, no. 3 (2024): 1816–1841, https://doi.org/10.1177/14759217231183715.

[11] L. Attard, C. J. Debono, G. Valentino, and M. Di Castro, "Tunnel Inspection Using Photogrammetric Techniques and Image Processing: A Review," *ISPRS Journal of Photogrammetry and Remote Sensing* 144 (2018): 180–188, https://doi.org/10.1016/j.isprsjprs.2018.07.010.

[12] E. Menendez, J. G. Victores, R. Montero, S. Martínez, and C. Balaguer, "Tunnel Structural Inspection and Assessment Using an Autonomous Robotic System," *Automation in Construction* 87 (2018): 117–126, https://doi.org/10.1016/j.autcon.2017.12.001.

[13] J. Jiang, W. Gan, Y. Hu, et al., "Real-time Monitoring Method for Unauthorized Working Activities above the Subway Tunnel Based on Ultra-weak Fiber Bragg Grating Vibration Sensing Array," *Measurement* 182 (2021): https://doi.org/10.1016/j.measurement.2021.109744.

[14] D. Hu, Y. Li, X. Yang, X. Liang, K. Zhang, and X. Liang, "Experiment and Application of NATM Tunnel Deformation Monitoring Based on 3D Laser Scanning," *Structural Control and Health Monitoring* 2023 (2023): 1–13, https://doi.org/10.1155/2023/3341788.

[15] Y. Jiang, L. Wang, B. Zhang, et al., "Tunnel Lining Detection and Retrofitting," *Automation in Construction* 152 (2023): https://doi.org/10.1016/j.autcon.2023.104881.

[16] A. H. Hartog, *An Introduction to Distributed Optical Fibre Sensors* (CRC Press, 2017).

[17] E. Lindsey, N. J. Lindsey, and E. R. Martin, *Fiber-Optic Seismology* (2021).

[18] P. Jousset, T. Reinsch, T. Ryberg, et al., "Dynamic Strain Determination Using Fibre-Optic Cables Allows Imaging of Seismological and Structural Features," *Nature Communications* 9, no. 1 (2018): 2509, https://doi.org/10.1038/s41467-018-04860-y.

[19] E. F. Williams, M. R. Fernández-Ruiz, R. Magalhaes, et al., "Distributed Sensing of Microseisms and Teleseisms with Submarine Dark Fibers," *Nature Communications* 10, no. 1 (2019): 5778, https://doi.org/10.1038/s41467-019-13262-7.

[20] M. W. Becker, C. Ciervo, M. Cole, T. Coleman, and M. Mondanos, "Fracture Hydromechanical Response Measured by Fiber Optic Distributed Acoustic Sensing at milli-Hertz Frequencies," *Geophysical Research Letters* 44, no. 14 (2017): 7295–7302, https://doi.org/10.1002/2017GL073931.

[21] Z. J. Spica, M. Perton, E. R. Martin, G. C. Beroza, and B. Biondi, "Urban Seismic Site Characterization by Fiber-Optic Seismology," *Journal of Geophysical Research: Solid Earth* 125, no. 3 (2020): 1–14, https://doi.org/10.1029/2019JB018656.

[22] R. Šturm, J. Polajnar, and M. Virant-Doberlet, *Practical Issues in Studying Natural Vibroscape and Biotic Noise* (Biotremology: studying vibrational behavior, 2019).

[23] C.-C. Zhang, B. Shi, J. Yin, T. Xie, Z. Wang, and S.-S. Zhang, "Seismic Wavefield and Strain Recordings on a 20-kilometer Dark Fiber Allow Detecting Mass Movement Events and Anthropogenic Activities Threatening a Natural Gas Pipeline," in *AGU Fall Meeting Abstracts* (New Orleans, LA, United States: American Geophysical Union, July 2021).

[24] K. J. Bergen, P. A. Johnson, M. V. de Hoop, and G. C. Beroza, "Machine Learning for Data-Driven Discovery in Solid Earth Geoscience," *Science* 363, no. 6433 (2019): https://doi.org/10.1126/science.aau0323.

[25] P. Ma, K. Liu, J. Jiang, Z. Li, P. Li, and T. Liu, "Probabilistic Event Discrimination Algorithm for Fiber Optic Perimeter Security Systems," *Journal of Lightwave Technology* 36, no. 11 (2018): 2069–2075, https://doi.org/10.1109/JLT.2018.2802324.

[26] X. Wang, Y. Liu, S. Liang, W. Zhang, and S. Lou, "Event Identification Based on Random Forest Classifier for Φ--OTDR Fiber-Optic Distributed Disturbance Sensor," *Infrared Physics & Technology* 97 (2019): 319–325, https://doi.org/10.1016/j.infrared.2019.01.003.

[27] C. Xu, J. Guan, M. Bao, J. Lu, and W. Ye, "Pattern Recognition Based on Enhanced Multifeature Parameters for Vibration Events in φ-OTDR Distributed Optical Fiber Sensing System," *Microwave and Optical Technology Letters* 59, no. 12 (2017): 3134–3141, https://doi.org/10.1002/mop.30886.

[28] J. Tejedor, J. Macias-Guarasa, H. Martins, J. Pastor-Graells, P. Corredera, and S. Martin-Lopez, "Machine Learning Methods for Pipeline Surveillance Systems Based on Distributed Acoustic Sensing: a Review," *Applied Sciences* 7, no. 8 (2017): 841, https://doi.org/10.3390/app7080841.

[29] R. Tangudu and P. K. Sahu, "Rayleigh Φ-OTDR Based DIS System Design Using Hybrid Features and Machine Learning Algorithms," *Optical Fiber Technology* 61 (2021): https://doi.org/10.1016/j.yofte.2020.102405.

[30] T.-Y. Zhang, B. Shi, C.-C. Zhang, T. Xie, J. Yin, and J.-P. Li, "Tunnel Disturbance Events Monitoring and Recognition with Distributed Acoustic Sensing (DAS)," *IOP Conference Series: Earth and Environmental Science* 861, no. 4 (2021): 042034, https://doi.org/10.1088/1755-1315/861/4/042034.

[31] Y. Zhang and Y. Yang, "Cross-validation for Selecting a Model Selection Procedure," *Journal of Econometrics* 187, no. 1 (2015): 95–112, https://doi.org/10.1016/j.jeconom.2015.02.006.

[32] Y. Ohta, T. Kobayashi, H. Tsushima, et al., "Quasi Real-Time Fault Model Estimation for Near-Field Tsunami Forecasting Based on RTK-GPS Analysis: Application to the 2011 Tohoku-Oki Earthquake (M W 9.0)," *Journal of Geophysical Research: Solid Earth* 117, no. B2 (2012): 1–16, https://doi.org/10.1029/2011JB008750.

[33] T. Maze, M. Agarwai, and G. Burchett, "Whether Weather Matters to Traffic Demand, Traffic Safety, and Traffic

schm, 2025, 1, Downloaded from https://onlinelibrary.wiley.com/doi/10.1155/ste/9780866 by Cochrane Czech Republic, Wiley Online Library on [21/03/2026]. See the Terms and Conditions (https://onlinelibrary.wiley.com/terms-and-conditions) on Wiley Online Library for rules of use; OA articles are governed by the applicable Creative Commons License

Operations and Flow," *Transportation Research Journal Board* 1948 (2006): 170–176, https://doi.org/10.3141/1948-19.

[34] D. M. Boore and E. M. Thompson, "Path Durations for Use in the Stochastic-Method Simulation of Ground Motions," *Bulletin of the Seismological Society of America* 104, no. 5 (2014): 2541–2552, https://doi.org/10.1785/0120140058.

[35] K. Dragomiretskiy and D. Zosso, "Variational Mode Decomposition," *IEEE Transactions on Signal Processing* 62, no. 3 (2014): 531–544, https://doi.org/10.1109/TSP.2013.2288675.

[36] F. Al-Badour, M. Sunar, and L. Cheded, "Vibration Analysis of Rotating Machinery Using Time-Frequency Analysis and Wavelet Techniques," *Mechanical Systems and Signal Processing* 25, no. 6 (2011): 2083–2101, https://doi.org/10.1016/j.ymssp.2011.01.017.

[37] P. Flandrin, G. Rilling, and P. Goncalves, "Empirical Mode Decomposition as a Filter Bank," *IEEE Signal Processing Letters* 11, no. 2 (2004): 112–114, https://doi.org/10.1109/LSP.2003.821662.

[38] J.-R. Yeh, J. S. Shieh, and N. E. Huang, "Complementary Ensemble Empirical Mode Decomposition: a Novel Noise Enhanced Data Analysis Method," *Advances in Adaptive Data Analysis* 02 (2010): 135–156, https://doi.org/10.1142/S1793536910000422.

[39] T. Zhang, C.-C. Zhang, B. Shi, Z. Chen, X. Zhao, and Z. Wang, "Artificial Intelligence-Based Distributed Acoustic Sensing Enables Automated Identification of Wire Breaks in Prestressed Concrete Cylinder Pipe," *Journal of Applied Geophysics* 224 (2024): https://doi.org/10.1016/j.jappgeo.2024.105378.

[40] H. Zou and T. Hastie, "Regularization and Variable Selection via the Elastic Net," *Journal of the Royal Statistical Society-Series B: Statistical Methodology* 67, no. 2 (2005): 301–320, https://doi.org/10.1111/j.1467-9868.2005.00503.x.

[41] P. Waldmann, G. Mészáros, B. Gredler, C. Fuerst, and J. Sölkner, "Evaluation of the Lasso and the Elastic Net in Genome-wide Association Studies," *Frontiers in Genetics* 4 (2013): 1–11, https://doi.org/10.3389/fgene.2013.00270.

[42] Z.-H. Zhou, *Ensemble Methods: Foundations and Algorithms* (CRC Press, 2012).

[43] R. Poli, J. Kennedy, and T. Blackwell, "Particle Swarm Optimization," *Swarm Intell* 1 (2007): 33–57, https://doi.org/10.1007/s11721-007-0002-0.

[44] D. Ramyachitra and P. Manikandan, "Imbalanced Dataset Classification and Solutions: a Review," *International Journal of Computing and Business Research* 5 (2014): 1–29.

[45] C. C. Zhang, B. Shi, K. Gu, et al., "Vertically Distributed Sensing of Deformation Using Fiber Optic Sensing," *Geophysical Research Letters* 45, no. 21 (2018): https://doi.org/10.1029/2018GL080428.

[46] C. Zhang, B. Shi, H. Zhu, B. Wang, and G. Wei, "Toward Distributed Fiber-Optic Sensing of Subsurface Deformation: A Theoretical Quantification of Ground-Borehole-Cable Interaction," *Journal of Geophysical Research: Solid Earth* 125 (2020): 0–3, https://doi.org/10.1029/2019JB018878.

[47] X. Yin, Q. Liu, X. Huang, and Y. Pan, "Real-time Prediction of Rockburst Intensity Using an Integrated CNN-Adam-BO Algorithm Based on Microseismic Data and its Engineering Application," *Tunnelling and Underground Space Technology* 117 (2021): https://doi.org/10.1016/j.tust.2021.104133.

[48] N. M. Shapiro, M. Campillo, L. Stehly, and M. H. Ritzwoller, "High-resolution Surface-Wave Tomography from Ambient Seismic Noise," *Science* 307, no. 5715 (2005): 1615–1618, https://doi.org/10.1126/science.1108339.

schm, 2025, 1, Downloaded from https://onlinelibrary.wiley.com/doi/10.1155/stc/9780866 by Cochrane Czech Republic, Wiley Online Library on [21/03/2026]. See the Terms and Conditions (https://onlinelibrary.wiley.com/terms-and-conditions) on Wiley Online Library for rules of use; OA articles are governed by the applicable Creative Commons License